International Journal of Control

ISSN: (Print) (Online) Journal homepage: https://www.tandfonline.com/loi/tcon20

Real-time target alignment system for high-power high-repetition rate laser operations using a five degree-of-freedom hybrid mechanism

Shah Karim , Samanta Piano , David Branson , Teguh Santoso , Richard Leach & Martin Tolley

To cite this article: Shah Karim , Samanta Piano , David Branson , Teguh Santoso , Richard Leach & Martin Tolley (2020): Real-time target alignment system for high-power high-repetition rate laser operations using a five degree-of-freedom hybrid mechanism, International Journal of Control, DOI: 10.1080/00207179.2020.1827297

To link to this article: https://doi.org/10.1080/00207179.2020.1827297

Published online: 04 Dec 2020.

INTERNATIONAL JOURNAL OF CONTROL
https://doi.org/10.1080/00207179.2020.1827297

Taylor & Francis
Taylor & Francis Group

Real-time target alignment system for high-power high-repetition rate laser operations using a five degree-of-freedom hybrid mechanism

Shah Karim[a], Samanta Piano[a], David Branson[b], Teguh Santoso[a], Richard Leach[a] and Martin Tolley[c]

[a]Manufacturing Metrology Team, Faculty of Engineering, University of Nottingham, Nottingham, UK; [b]Advanced Manufacturing Research Group, Faculty of Engineering, University of Nottingham, Nottingham, UK; [c]Central Laser Facility, Science and Technology Facilities Council, Oxfordshire, UK

ABSTRACT

This paper presents a real-time position control solution for the targets used in the high-repetition rate laser operations of high-power laser facilities. The control system is designed based on an Abbe-compliant, in-process position measurement system of targets, employing a plane mirror interferometer and a five degree-of-freedom hybrid mechanism. An error model is developed to characterise the position feedback information of target for a high-repetition rate process to determine the effects of the non-collocation of the sensor's measurement point and target on the control system's performance – a challenge for the real-time position control of targets. Behaviour of the control system is investigated with the error model and experimental data. It is found that a controller's position compensation scheme can be ineffective due to the erroneous position feedback as a result of the non-linear position information associated with the non-collocated measurement point and the actual target. To solve the problem, an angular compensation technique is proposed.

ARTICLE HISTORY
Received 29 January 2020
Accepted 13 September 2020

KEYWORDS
Real-time position and orientation control; in-process metrology; hybrid mechanism; target position feedback; position and angular compensation; complaint and non-complaint feedback information

1. Introduction

The position accuracy of a target (tool or end-effector, but hereafter just called target), is one of the most important requirements for many precision systems, such as ultra-precision machine tools, coordinate measuring machines and surgical robots. Positional accuracy is generally achieved by carrying out one or more of these processes: design, following precision engineering principles; calibration, requiring steps, such as kinematic modelling, error identification and error compensation; and compensation for the target's path (or trajectory), requiring in-process measurement of the position of the target while the operation is taking place (i.e. real-time compensation) (Bosmans et al., 2017; Buice, 2018; Karim, Piano, Leach, Branson, et al., 2018; Karim, Piano, Leach, & Tolley, 2018; Schmitt et al., 2013; Schmitt et al., 2012; Schwenke et al., 2008; Ruijl, 2001; Ramesh et al., 2000; Sartori & Zhang, 1995). Real-time compensation using in-process metrology has been playing an increasingly important role in recent years in the process chain for manufacturing of precision workpieces with complex shapes and/or tight tolerances (Schmitt et al., 2012; Schmitt et al., 2013). Beyond the task of quality control for workpieces, in-process metrology has proven effective for manufacturing process control, by allowing optimisation of the process and the machine tool settings (Gao et al., 2019; Hansen et al., 2006). However, developing an instrument for in-process measurements comes with many challenges, e.g. appropriate mounting of the sensor in the manufacturing machine, high measurement speeds to follow the manufacturing operation and avoidance of environmental disturbances (Colledani et al., 2014; Syam et al., 2019; Yang & Zhang, 2018). For these challenges, most in-process measurement solutions are application-specific, and research covering different aspects of in-process metrology, such as instrumentation, acquisition and calibration, is increasing (Gao et al., 2019). The research presented in this paper aims to develop an effective solution for real-time target position compensation for high-power laser operations.

Large-scale facilities with high-power lasers (petawatt class lasers) need to operate at high-repetition rates to utilise the full potential of the lasers, which comes with many engineering challenges (Booth et al., 2014; Spindloe et al., 2011). One such challenge is the requirement for positioning and orientating the fresh targets at the laser beam focus with an accuracy of a few micrometres at a rate of at least a few hertz (Booth et al., 2014; Spindloe et al., 2011; Symes et al., 2014; Tolley & Spindloe, 2013). For example, clinically relevant experiments require several thousands of laser shots, which demand for an automated target positioning system. One method of automated positioning of nano-scale targets was reported by Gao et al. (2017). With the use of a six-axis hexapod, a specially designed target wheel, a microscope and a confocal chromatic displacement sensor, they achieved a target positioning accuracy of around 5 μm in all spatial dimensions at 0.5 Hz repetition rate; but this method represents a pre-calibrated compensation for target's positional deviations. Another method of automated target alignment (positioning and orientation) can be found in the

CONTACT Shah Karim shah.karim@nottingham.ac.uk Manufacturing Metrology Team, Faculty of Engineering, University of Nottingham, Nottingham, NG8 1BB, UK

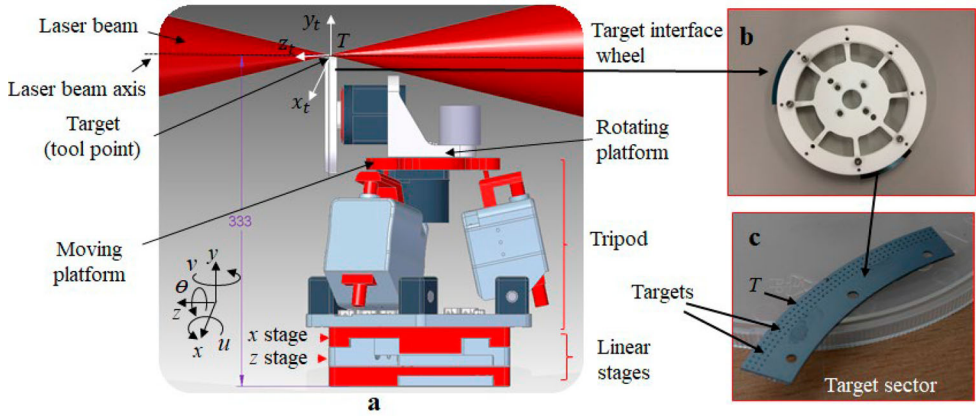

Figure 1. HAMS for high-power high-repetition rate laser operations: (a) HAMS with the target interface wheel; (b) target interface wheel with two replaceable target sectors; (c) targets patterned around the circumference of a target sector [adapted from Karim, Piano, Leach, and Tolley (2018)].

form of an integrated target solution developed by the Central Laser Facility (CLF) (Booth et al., 2014; Spindloe et al., 2011; Symes et al., 2014). The target solution of the CLF, known as the 'High Accuracy Microtarget Supply' (HAMS) system, uses a number of identical targets manufactured with MEMS technology and delivers the targets to the laser focus within specifications at high speed (hertz level). Automated target alignment using HAMS is the focus of this paper.

The motion stages, the key component of HAMS as shown in Figure 1*a*, form a five degree-of-freedom hybrid mechanism: a linear *xz* stages and a tripod, which is a parallel mechanism (the description of the motion stages is given elsewhere (Karim, Piano, Leach, & Tolley, 2018)). The motions of the hybrid mechanism are used for high-speed (hertz level) positioning of the target at the laser focal spot within the specifications (i.e. within $\pm 10\ \mu$m of the centre of the 300 μm diameter target in the *x* and *y* directions and within $\pm 4\ \mu$m of the laser focus in the *z* direction) – see Figure 1 (Booth et al., 2014; Karim, Piano, Leach, & Tolley, 2018). While the *x* and *y* specifications are to ensure that the laser hits the target without damaging the surroundings, the *z* specification is to ensure that the targets receive the highest intensity of the laser beam. It is also important that the targets are positioned perpendicular to the laser beam during operation.

The target alignment at high-repetition rate depends on the ability of the motion stages of HAMS to generate the translational and rotational motions to locate the target with the required accuracy and repeatability. The performance of the parallel mechanism of HAMS, in terms of its ability to achieve high-accuracy target positioning, is described elsewhere (Karim, Piano, Leach, Branson, et al., 2018; Karim, Piano, Leach, & Tolley, 2018). However, high-accuracy target alignment in high-repetition rate operation means that a real-time position compensation method is required to maintain the target's reference position and plane throughout the operation. This can be achieved by the HAMS controller with the use of a closed-loop control when the target positions (and ideally orientations) are known throughout the operation. This measurement requirement can be fulfilled by using in-process metrology but comes with a number of challenges. For laser operation, the major challenges are: 1. adverse operating conditions (electro-magnetic pulse of the laser) for the sensor, 2. space constraints inside the laser chamber and 3. the measurement speed required to followthe high-repetition rate. Furthermore, the necessity for the targets to be placed at the laser focus and perpendicular to the laser beam (Figure 1*a*) means that information about both the target's position and orientation are needed by the controller to make the necessary compensations for the target alignment. Irrespective of the applications (laser or non-laser), in-process measurement of the target's orientation can be difficult, as comprehensive information about the target's location is required throughout the operation.

This paper reports the development of a closed-loop control system using an Abbe-complaint, in-process position measurement system for real-time alignment of the targets for high-repetition rate laser operations. The design principles of the in-process target position measurements are discussed, followed by the derivation of a model showing the relationship between the positional deviations of the target, which form the feedback information to the sensor, and the error sources related to the high-repetition rate system. The hardware set-up, control scheme of the closed-loop system and the experimental procedure are described. Implementation issues with the closed-loop control are discussed in light of the experimental results and the model, which led to strategies for improving the performance of the closed-loop control for the real-time target alignment. Lastly, some examples are given to demonstrate the applicability of the model for wider precision applications.

2. Design of the control system for high-repetition rate laser operations

Considering the performance of a positioning system in terms of the positional accuracy of the target, the following three locations of the system's elements with respect to the system's coordinate system are critical for closed-loop control (Schmidt et al., 2014):

- the actuator's location;
- the sensor's location; and
- the target's location.

For closed-loop control of a precision positioning system, the location of the sensor in the system is an important consideration, because the locations of the actuators and sensors influence the 'observability' and 'controllability' of an active control positioning system (Schmidt et al., 2014; Yang & Lee, 1993). In the case that the positioning system's sensor and actuator are non-collocated, which is often the case, the functionality of the positioning system can be impaired. In such cases, the controller is unable to improve the system's dynamic behaviour due to closed-loop instability or a time-delay in the feedback loop (Bruant et al., 2010; Yang & Lee, 1993). Furthermore, non-collocation of the sensor and the target may result in Abbe errors in the position measurement of the target, which in turn mean that the controller's compensation for the target position, based on the sensor's measurement, can be ineffective, leading to inaccuracy in target re-positioning during high-repetition rate operation.

The design of the position measurement system for the target is examined in the following sections in light of the Abbe principle. The development of an analytical model is then outlined to show the relationship between the target position feedback (i.e. the z positional deviations of the target with respect to its reference position) and the factors affecting the feedback.

2.1 In-process position measurement for the high-repetition rate operation: applying the Abbe principle

The generalised Abbe principle, reformulated by Bryan (1979), states that 'the path of the effective point (EP) of a displacement measuring system should be collinear with the path of the functional point (FP) whose displacement is to be measured. If collinearity is not possible, either the slideways that transfer the displacement must be free of angular motion or angular motion data must be used to calculate the consequences of the offset' (Bosmans et al., 2017). In this respect, one technique for achieving an Abbe complaint measurement system for a two or three degree of freedom (DOF) system is to keep the FP stationary with respect to the reading head of the sensor (EP), when the FP is always coincident with the path of the EPs of the sensor during the measurement. This configuration is attainable only if the sensor measures the movement of the target surface surrounding the workpiece or the motion stages, at the same time allowing the target surface to move in a direction perpendicular to the sensor's measurement direction (Bosmans et al., 2017; Ruijl, 2001). A measurement configuration based on the above principle was proposed by Bosmans et al. (2017) to develop an ultra-precision, Abbe-complaint position measurement system with linear encoders.

The measurement configuration stated above can be applied to develop an Abbe compliant measurement system to measure the positional deviation of a target T (FP in this case) located at the target wheel rotating at a certain speed. For example, in Figure 2 consider $\overrightarrow{WT}$ as a vector representing the reference position and orientation of the target T with the coordinate position (x_t, y_t, z_t). When the target at position T' moves to T, the coordinate position of T' has to be within x, y and z specifications of (x_t, y_t, z_t). However, if error motions arise due to some disturbances (e.g. the kinematic errors of the wheel), T' will reach T_{err}, generating a positional error $\overrightarrow{TT}_{err}$ at point T. Provided this error motion along the z axis can be detected by the interferometer and then fed back to the controller for compensation, the target will be repositioned at T before the laser hits the target. In this way, all the targets around the target wheel will be within the z specification of the laser focus (only the z positional deviation is considered in this paper, since z is considered as the sensitive direction for the target alignment). If plane mirrors, as shown in Figure 3, can be placed around the circumferential edge of the wheel (this mirror setting will be referred as 'target position setting' henceforth) and a plane mirror interferometer (Renishaw model XL-80) is used to measure the relative movement between the sensor and target point T, then the FP and EP become coincident. However, it is very difficult to place the plane mirrors around the circumferential edge of the wheel along with the target sectors. Therefore, plane mirrors are placed at the front face of the wheel around the circumference, functioning as a target surface (this mirror setting will be referred as 'mirror position setting' henceforth) as described before. In this arrangement, although the EP of the mirror position setting (M on the plane mirror as shown in Figure 3) is at some offsets to the FP of the target position setting (T as shown in Figure 3), the interferometer measures the movement of the target surface while allowing the target surface to move in a direction perpendicular to the interferometer's measurement direction (along x direction as shown in Figure 3) during the wheel rotation.

2.2 Positional deviation of target during wheel rotation: model

An equation needs to be found that describes the positional deviation of the target in the z direction when the target moves from point T' to point T during wheel rotation, as shown in Figure 4. T is represented by a coordinate system $x_T y_T z_T$ whose position is (x_t, y_t, z_t) with respect to the machine's reference coordinate $x_w y_w z_w$. In the error-free condition, (x_t, y_t, z_t) will be the reference position of the target, while T' is represented by a coordinate system $x_{T'} y_{T'} z_{T'}$ whose position is $(x_{t'}, y_{t'}, z_{t'})$ with respect to the machine's reference coordinate $x_w y_w z_w$. T' is positioned at an angular distance θ from T, and the equation to be derived will provide the positional deviation of the target for a complete wheel rotation.

The positional deviation of the target is generated from the interferometer's measurement of the change of z_t of the reference point (x_t, y_t, z_t), when all the T' points around the circumference of the wheel pass through the point T in a complete rotation of the wheel. The positional deviation response shows the effect of the error motions related to the wheel rotation, arising from different error sources, such as geometric and dynamic disturbances. Assuming that the displacement measurement by the interferometer takes place in a controlled environment and, therefore, has negligible random errors from environmental disturbances, the positional deviation of the target in the z direction can be described in terms of the 'face runout' of the wheel as a result of the geometric disturbances. Face runout can be defined as the total displacement measured parallel to the z reference axis at a specified radial location of

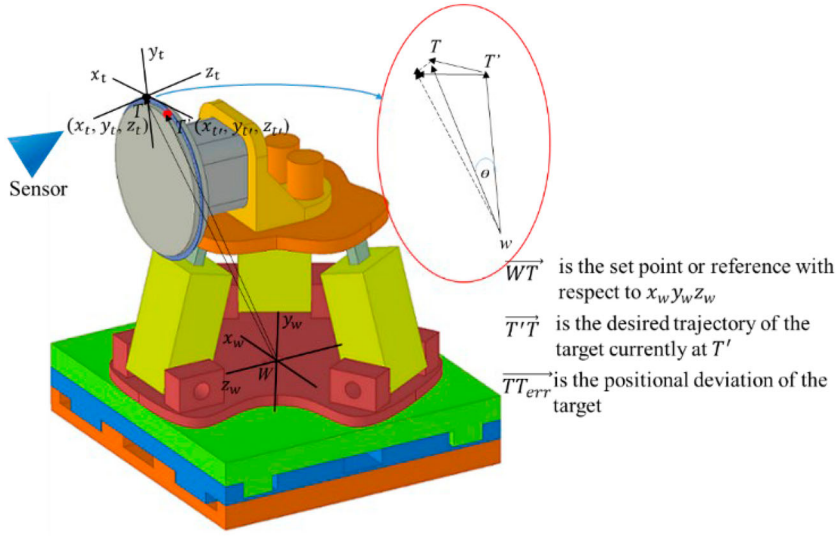

Figure 2. Concept of the closed-loop control for *z* position compensation.

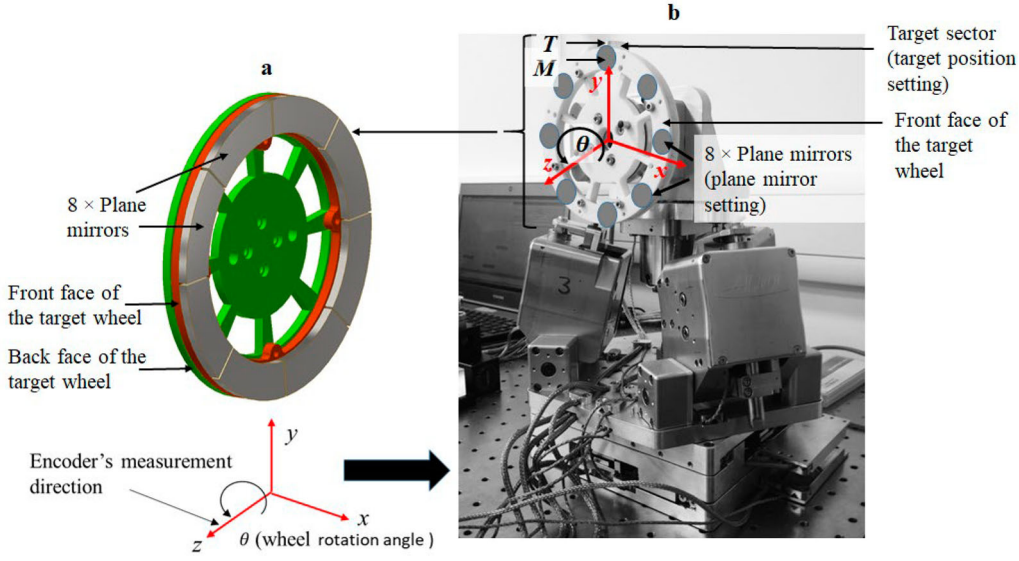

Figure 3. Plane mirror position (a) ideal mirror setting (b) actual mirror setting.

the wheel by an instrument sensing against a moving surface or moved with respect to a fixed surface (Slocum, 1992). Assuming that a reference coordinate $x_{0'}y_{0'}z_{0'}$ (Figure 4*a*) is placed at point *O'* of the interferometer's quarter-wave plate, from which the measurement beam emerges from the interferometer, the relative motion between the reference coordinates of the interferometer (i.e. $x_{0'}y_{0'}z_{0'}$) and the wheel (i.e. $x_T y_T z_T$) measured by the interferometer will determine the face motion of the wheel.

The coordinate systems are placed at points of interest within the system (the motion stages of HAMS and the interferometer) as shown in Figure 4, namely $x_C y_C z_C$ at the centre of the wheel *C* and $x_0 y_0 z_0$ at point *O* (*O* is perpendicularly below *Ó* on the same plane). Note that in Figure 4 point *M* of the mirror, which has the coordinate $x_M y_M z_M$ placed at (x_m, y_m, z_m), corresponds to target point *T*. This means that offsets exist between the FP (i.e. *T*) and EP (i.e. *M*) in the *y* and *z* directions, called *l* and *h* respectively. Ideally, *T* and *M* should be aligned (i.e. no offset in the *x* direction) to minimise Abbe error. However, an offset *s* in the *x* direction is also considered in the model for the sake of generality.

Consider that *T* is directly above the centre of the wheel *C*. If a plane mirror can be placed at *T* so that the interferometer can measure the *z* displacement of *T* (ideally, the interferometer plane should be parallel to the wheel's plane), the interferometer will read the value $O'T$, which is equal to $(z + l)$, where *z* is the perpendicular distance between *O* of the interferometer plane and the centre of the wheel *C* (see Figure 4*a*), and *l* is the perpendicular distance in the *z* direction between point *M* and target *T* (see Figure 4*c*).

The positional deviation of the target in terms of the wheel's face runout can be derived using a homogeneous transformation matrix (HTM) (Seugling, 2018). In the current analysis, it is possible to define an HTM for each successive position and orientation change of the mirror, with respect to the fixed $x_{o'}y_{o'}z_{o'}$ coordinate of the interferometer, to determine the final position of the target. This is because the reflected beam from the plane

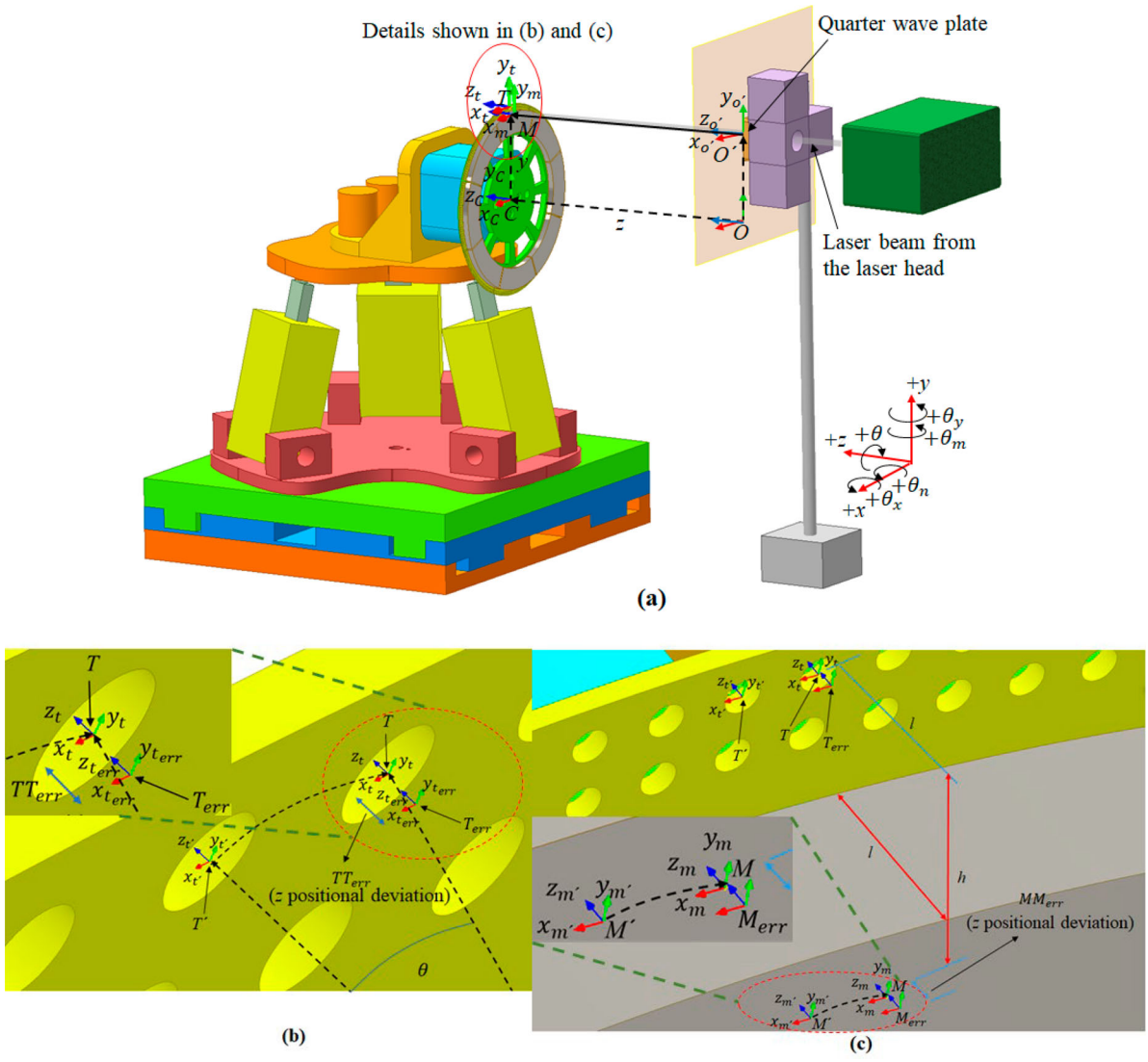

Figure 4. Coordinate systems for the error model (a) with the effective and functional points shown in (b) and (c).

mirror (at the target position or mirror position setting) entering the interferometer is directly affected by the position and orientation change of the plane mirror with respect to $x_{o'}y_{o'}z_{o'}$.

In the case that the wheel does not have any face motion (i.e. error-free condition) and T' corresponds to T as shown in Figure 4*a* and *b*, the position and orientation of T' with respect to the coordinate $x_{o'}y_{o'}z_{o'}$ ($x_{o'}y_{o'}z_{o'}$ and $x_oy_oz_o$ have the same orientation) can be represented by the following HTM (z distance measured by the interferometer should remain unchanged, since T and T' are the same point of the mirror):

$$T^O_{T_{no\ error}} = T^O_{Target}T(\theta), \tag{1}$$

where T^O_{Target} is the HTM to describe the position of the target with respect to $x_{o'}y_{o'}z_{o'}$ when there is no wheel rotation, and is given by

$$T^O_{Target} = \begin{bmatrix} 1 & 0 & 0 & s \\ 0 & 1 & 0 & y+h \\ 0 & 0 & 1 & z+l \\ 0 & 0 & 0 & 1 \end{bmatrix}, \tag{2}$$

where y is the radius of the wheel or the distance between C and M, as shown in Figure 4. $T(\theta)$ is the HTM to describe the rotation of wheel about z_C of $x_Cy_Cz_C$, and is given by

$$T(\theta) = \begin{bmatrix} \cos\theta & \sin\theta & 0 & 0 \\ -\sin\theta & \cos\theta & 0 & 0 \\ 0 & 0 & 1 & 0 \\ 0 & 0 & 0 & 1 \end{bmatrix} \tag{3}$$

By combining equations (2) and (3), $T^O_{T_{no\ error}}$ in equation (1) will have the following form

$$T^O_{T_{no\ error}} = \begin{bmatrix} \cos\theta & \sin\theta & 0 & (h+y)\sin\theta + s\cos\theta \\ -\sin\theta & \cos\theta & 0 & (h+y)\cos\theta - s\sin\theta \\ 0 & 0 & 1 & z+l \\ 0 & 0 & 0 & 1 \end{bmatrix}. \tag{4}$$

The face motion of the wheel, expressed in terms of the positional deviation of the target T, results in two rotational error motions that are generated due to imperfect wheel rotation about the z_C axis of $x_Cy_Cz_C$. One error motion (θ_x) is the tip error that represents a rotation about x_C of $x_Cy_Cz_C$, and the

other is the tilt error (θ_y) that represents a rotation about y_C of $x_Cy_Cz_C$. Since the face motion distorts the ideal wheel rotation path, when the wheel rotates, a point T' on the wheel reaches to point T_{err} instead of point T (see Figure 4*b*), resulting in the change in the z distance measured by the interferometer. The position and orientation of T_{err} with respect to the coordinate $x_{o'}y_{o'}z_{o'}$ ($x_{o'}y_{o'}z_{o'}$, $x_oy_oz_o$, $x_Cy_Cz_C$, $x_Ry_Rz_R$ and $x_Ty_Tz_T$ have the same orientation at the outset of the wheel rotation) can be represented by the following HTM

$$T^O_{T_{err}} = T^O_C T(\theta_n)T(\theta_m)T(\theta_y)T(\theta_x)T(\theta)T^C_T, \tag{5}$$

where T^O_C is the distance between C and O with respect to $x_oy_oz_o$, and is given by

$$T^O_C = \begin{bmatrix} 1 & 0 & 0 & 0 \\ 0 & 1 & 0 & 0 \\ 0 & 0 & 1 & z \\ 0 & 0 & 0 & 1 \end{bmatrix}. \tag{6}$$

$T(\theta_n)$ is the misalignment of the mirror described by the rotation θ_n about the x_C axis of coordinate $x_Cy_Cz_C$, and is given by

$$T(\theta_n) = \begin{bmatrix} 1 & 0 & 0 & 0 \\ 0 & \cos\theta_n & -\sin\theta_n & 0 \\ 0 & \sin\theta_n & \cos\theta_n & 0 \\ 0 & 0 & 0 & 1 \end{bmatrix}. \tag{7}$$

$T(\theta_m)$ is the misalignment of the mirror described by the rotation θ_m about the y_C axis of coordinate $x_Cy_Cz_C$, and is given by

$$T(\theta_m) = \begin{bmatrix} \cos\theta_m & 0 & \sin\theta_m & 0 \\ 0 & 1 & 0 & 0 \\ -\sin\theta_m & 0 & \cos\theta_m & 0 \\ 0 & 0 & 0 & 1 \end{bmatrix}. \tag{8}$$

$T(\theta_y)$ is the tilt error motion of the wheel with respect to $x_{o'}y_{o'}z_{o'}$ or $x_Cy_Cz_C$, and is given by

$$T(\theta_y) = \begin{bmatrix} \cos\theta_y & 0 & \sin\theta_y & 0 \\ 0 & 1 & 0 & 0 \\ -\sin\theta_y & 0 & \cos\theta_y & 0 \\ 0 & 0 & 0 & 1 \end{bmatrix}. \tag{9}$$

$T(\theta_x)$ is the tip error motion of the wheel with respect to $x_{o'}y_{o'}z_{o'}$ or $x_Cy_Cz_C$, and is given by

$$T(\theta_x) = \begin{bmatrix} 1 & 0 & 0 & 0 \\ 0 & \cos\theta_x & -\sin\theta_x & 0 \\ 0 & sin\theta_x & \cos\theta_x & 0 \\ 0 & 0 & 0 & 1 \end{bmatrix}. \tag{10}$$

T^C_T is the offset between C and T with respect to $x_Cy_Cz_C$, and is given by

$$T^C_T = \begin{bmatrix} 1 & 0 & 0 & s \\ 0 & 1 & 0 & y+h \\ 0 & 0 & 1 & l \\ 0 & 0 & 0 & 1 \end{bmatrix}. \tag{11}$$

After substituting the values from equations (3) and (6) to (11) into equation (5), and then subtracting equation (1) from equation (5) provides the HTM T_{error}, which represents the position and orientation deviation of the target when it moves from T' to T. Therefore,

$$T_{error} = \begin{bmatrix} A_1 & B_1 & C_1 & D_1 \\ A_2 & B_2 & C_2 & D_2 \\ A_3 & B_3 & C_3 & D_3 \\ 0 & 0 & 0 & 1 \end{bmatrix} \tag{12}$$

where $A_1, A_2, A_3, B_1, B_2, B_3, C_1, C_2, C_3, D_1$ and D_2 (i.e. equations (13) to (23)) are shown in Appendix 1,

and

$$\begin{aligned} D_3 = {} & (h+y)(\sin\theta\cos\theta_n\sin(\theta_y+\theta_m) \\ & + \cos\theta(\cos\theta_x\sin\theta_n + \sin\theta_x\cos\theta_n\cos(\theta_y-\theta_m)) \\ & - s(\cos\theta\cos\theta_n\sin(\theta_y+\theta_m) - \sin\theta(\cos\theta_x\sin\theta_n \\ & + \sin\theta_x\cos\theta_n\cos(\theta_y-\theta_m)) \\ & - l(\sin\theta_n\sin\theta_x - \cos\theta_x\cos\theta_n\cos(\theta_y-\theta_m)) - l. \end{aligned} \tag{24}$$

Equation (24) represents the positional deviation of the target TT_{err} in the z direction as measured by the interferometer. To derive a simpler form of equation (24), assume that the misalignments of the mirror are negligible, which means θ_m and θ_n are zero (the effects of misalignment and their avoidance are discussed in section 4.2). Also, assume that s in equation (24) is zero, which means M and target point T are aligned, as shown in Figure 4. Therefore, equation (24) becomes

$$\begin{aligned} z_{error} = TT_{err} = {} & (h+y)(\sin\theta\sin\theta_y + \cos\theta\sin\theta_x\cos\theta_y) \\ & + l\cos\theta_x\cos\theta_y - l. \end{aligned} \tag{25}$$

Taking $(h+y)\sin\theta_y = E_r\cos\alpha$ and $(h+y)\sin\theta_x\cos\theta_y = E_r\sin\alpha$, equation (25) can be re-written as the periodic function equation

$$z_{error} = E_r\sin(\theta+\alpha) + l\cos\theta_x\cos\theta_y - l \tag{26}$$

where

$$E_r = (h+y)\sqrt{((\sin\theta_y)^2 + (\sin\theta_x\cos\theta_y)^2)}, \tag{27}$$

and

$$\alpha = \tan^{-1}\frac{\sin\theta_x}{\tan\theta_y}. \tag{28}$$

The sine function in equation (26) relates the rotational distance travelled by the wheel (i.e. θ) to the corresponding positional deviation of the target in terms of wheel's error motions θ_x and θ_y. Note that $(h+y)$ in equation (27) becomes $(h+y)/\cos\theta$ at angle θ and is subject to change by θ_x and θ_y. So, equation (27) becomes

$$E_r = \frac{(h+y)\sqrt{((\sin\theta_y)^2 + (sin\theta_x\cos\theta_y)^2)}}{\cos\theta}. \tag{29}$$

From the model described, the following observations are important for the analysis of the experimental data in section 5.

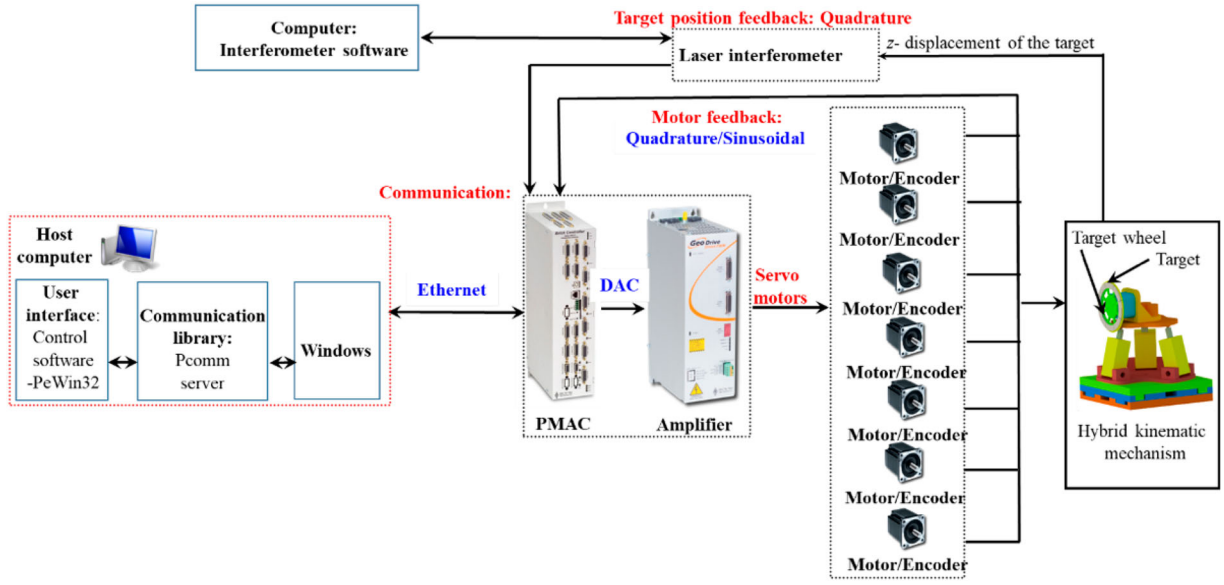

Figure 5. Hardware set-up for the closed-loop control of the target.

1. As mentioned before, since it is practically very difficult to place the mirror exactly at the target position T (i.e. target position setting) to read the displacement and, therefore, the mirrors are placed at the front face of the wheel around the circumference (i.e. mirror position setting), the resultant position deviation at point M as read by the interferometer will be determined by

$$z_{erroratM} = E_r \sin(\theta + \alpha) \tag{30}$$

where

$$E_r = \frac{y\sqrt{((\sin\theta_y)^2 + (\sin\theta_x \cos\theta_y)^2)}}{\cos\theta}. \tag{31}$$

The difference between equations (26) and (30), as shown in equation (32), represents the error in the target position feedback because of the use of the mirror position setting (EP) in the control system, i.e.

$$z_{feedbackerror} = \left(\frac{h\sqrt{((\sin\theta_y)^2 + (\sin\theta_x \cos\theta_y)^2)}}{\cos\theta} \sin(\theta + \alpha)\right) + (l\cos\theta_x \cos\theta_y - l). \tag{32}$$

3. Design of the closed-loop control system

The hardware set-up for the closed-loop system is shown in Figure 5, and the control scheme is presented in Figure 6. The HAMS motion stages use Delta Tau's multi-axis motion control system (Turbo PMAC) to control the seven servo motors (three for the tripod, two for the two linear stages, one for the rotating platform and one for the wheel rotation – see Figure 1*b*) of the motion stages with the use of the quadrature signals generated from the seven encoders of the respective motors. The eighth encoder channel of the controller accepts the quadrature signal from the interferometer to provide the real-time position information about the target. Although the position encoders of the motion stages and the interferometer are both incremental encoders, the resolution of the encoders of the motion stages is not as high as the resolution of the interferometer. Therefore, the quadrature signal generated by the interferometer is converted to the equivalent encoder counts through the use of an encoder conversion table (a characteristic feature of the Turbo PMAC controller); the counts can then be used by the controller's servo motors for the position compensations ('Delta Tau Data System,' 2008).

As part of setting the control system, a motion programme was written in the controller's language, using the controller's various functional parameters, to run the target wheel at a specified speed, read the position information from the interferometer and then compensate the position deviations by actuating the motion stage/s. The simplified flowchart of the motion programme is shown in Figure 7.

4. Experimental validation of the closed-loop design for the high-repetition rate laser operation

4.1 Experimental procedure

Experiments were carried out to verify the design of the closed-loop control, as described in sections 2.1 and 3, for real-time target alignment for high-repetition rate laser operations. The experiments can be divided into two groups: open-loop and closed-loop, while the main objectives are as follows.

(1) For the open-loop experiments: evaluate, with respect to the required positional accuracy of target (±4 μm in the z direction), the high-repetition rate system's behaviour in open-loop control by measuring the z positional deviations (magnitudes and directions) for a complete wheel rotation.
(2) For closed-loop experiments:
   (a) find a functional closed-loop design capable of generating the position compensations with the target position feedback; and

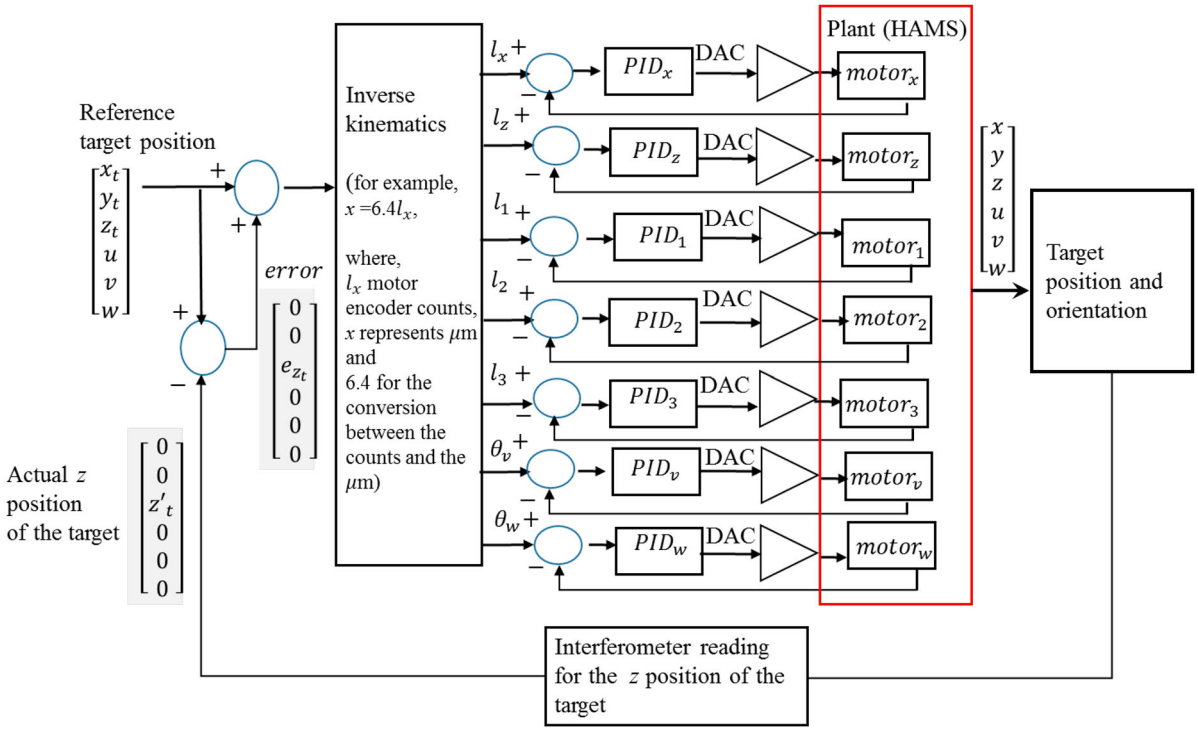

Figure 6. Control diagram of the closed-loop control for HAMS motion stages.

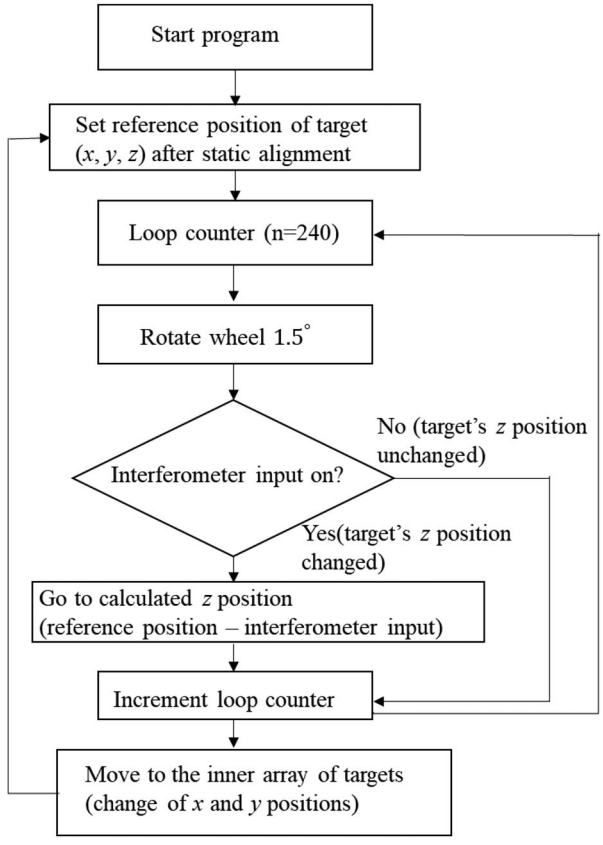

Figure 7. Simplified flow-diagram of the motion programme for the high-repetition rate operations.

(b) find an optimised closed-loop design capable of producing the necessary compensations to position the targets within the z position specification of the reference position.

4.1.1 Open-loop experiments

The set-up of the experiment is shown in Figure 4*a*, and the procedure of the target position measurement using the mirror interferometer is briefly outlined in sections 2.1. For the mirror position setting or EP (Figure 3 and 4), eight square plane mirrors (Thor Lab's 1' ×1' broadband dielectric mirror, 400 nm to 750 nm) were attached to the wheel at the angular positions 0°, 45°, 90°, 135°, 180°, 225°, 270° and 315°, covering a total angular distance of 189° of 360° of the wheel's circumference (see Figure 3 and 4). For the target position setting of FP (Figure 3 and 4), eight mirrors were placed around the circumferential edge of the wheel, maintaining the alignment with the corresponding eight mirror positions of the mirror position setting. The position measurements were taken at 0.5 Hz, representing 0.5 Hz repetition rate laser operation, which means there was a 2 s time-gap for each repetition, during which period a target moves from a position to the next position of the wheel (i.e. 1.5°).

4.1.2 Closed-loop experiments

The same interferometer set-up as described in section 4.1.1 was used to find a functional closed-loop design. With a functional closed-loop control system (see section 3 and Figure 5 and 6), a series of experiments – mainly to improve the motion

programme (Figure 7) for the compensation – were carried out to find the optimal condition/s at which ±4 μm position accuracy could be achieved. As will be shown in section 5, the investigation of the issues of the closed-loop control system led to suitable compensation techniques (angular compensation) for the target's alignment for the high-repetition rate operations. All closed-loop experiments were carried out at 0.5 Hz repetition rate.

4.2 Measurement uncertainties

The experimental results related to z position measurements are subject to some sources of measurement uncertainties, for example:

- errors from the conversion of the interferometer's quadrature signal to equivalent counts of the controller;
- accuracy of the motion of the z position stage; and
- misalignment of the plane mirrors that may cause parallel and/or orthogonality errors.

The interferometer's quadrature signal for position is converted to equivalent counts for the position measurement of the servo loop of the controller. Comparison of a number of z displacements measured by the interferometer and the controller's encoder (in terms of counts) shows that 1 μm for the interferometer is equivalent to 991 nm for the controller's encoder. Considering that the HAMS with closed-loop control will not show a positional deviation of more than ±5 μm during the wheel rotation, the maximum error related to the equivalent counts of the controller's encoder will be 45 nm. Furthermore, considering the positional accuracy of the z stage is ±2 μm for 25 mm travel (from supplier's data-sheet), the uncertainty related to the accuracy of the travelled distance in the z direction is negligible, since the controller's compensation will not exceed ±5 μm.

Although the parallel and orthogonality errors should be avoided as much as possible, it is worth mentioning the unique benefit of using a plane mirror interferometer for position measurements. In the plane mirror interferometer, the double pass of the laser beam to the plane mirror with retro reflection actually compensates a tilt of the mirror (Badami & deGroot, 2013).

5. Results and discussion

5.1 Characterisation of the high-repetition rate process in the open-loop system

For the high-repetition rate operation in open-loop control, the study of the z positional deviations at EP and FP essentially indicates a 'wheel characterisation' process, since the errors of the wheel are mapped through this process.

Figure 8 shows the profiles of the position feedback (z positional deviations) for eight locations of the wheel, as discussed in section 4.1. The feedback, as shown in Figure 8, has two components: the magnitude and the direction of the z positional deviation. Based on the position feedback from EP and FP (i.e. mirror and target position settings), two types of behaviour of the system can be observed during a complete wheel rotation.

(1) At some locations of the wheel (0°, 45°, 90°, 180° and 225° as shown in Figure 8), the position feedback from EP does not comply with the feedback from FP (the term 'non-compliance' is used henceforth to indicate this). In all such cases, the directions and magnitudes of the z position deviations are non-compliant to each other.
(2) At some locations of the wheel (135°, 270° and 325°) as shown in Figure 8, the position feedback from both EP and FP comply with each other (the term 'compliance' is used henceforth). At location 325°, both the magnitude and direction of the z positional deviation are almost the same for EP and FP. However, at locations 135° and 270°, the positional deviations at EP and FP initially appear to comply with each other but deviate (in magnitude and/or direction) at the later stage with further rotation of the wheel.

5.2 Performance evaluation of the closed-loop design

Following the examination of the system's open-loop characteristics, the closed-loop behaviour was studied by evaluating the control system's performances in terms of its ability to reposition the target within ±4 μm of the reference position. Analysis of the experimental results showed that the controller's position compensations were able to reposition the target within ±1.7 μm of the reference position by using the position feedback (z positional deviation) from EP or FP (indicated by the compensation values of the O and P profiles in Figures 9 and 10). However, although the accuracy level (±1 μm) indicates that the closed-loop system is functioning well, the results of the closed-loop experiments highlight the problems related to the position feedback from EP and FP (see section 5.1). The key observations, as shown in Figure 9 and 10, are the following.

(1) Figure 9 and 10 show typical behaviours of the closed-loop system for the complaint and non-complaint cases, respectively. These two characteristic behaviours indicate that, while at some locations the position feedback from EP (the mirror position setting) can be representative (check M and N profiles of Figure 9) of the actual positional deviation of the target or FP (with ±1 μm error as indicated by profile Q in Figure 9), the position feedback from EP cannot represent (see M and N profiles of Figure 10) the target position or FP at other locations (i.e. non-complaint cases).
(2) For the non-complaint cases, the compensation by the controller based on the feedback from EP does not produce any benefit, and the positional deviation of the target (FP) remains uncompensated, as indicated by profile Q of Figure 10. Note that profile P of Figure 10 represents the controller's compensation based on the position feedback from EP.
(3) The zigzag upward or downward trend (Figure 9 and 10) of the positional deviation curves indicates that the plane of the wheel with respect to the interferometer's measurement beam is changing with each wheel rotation angle (1.5°),

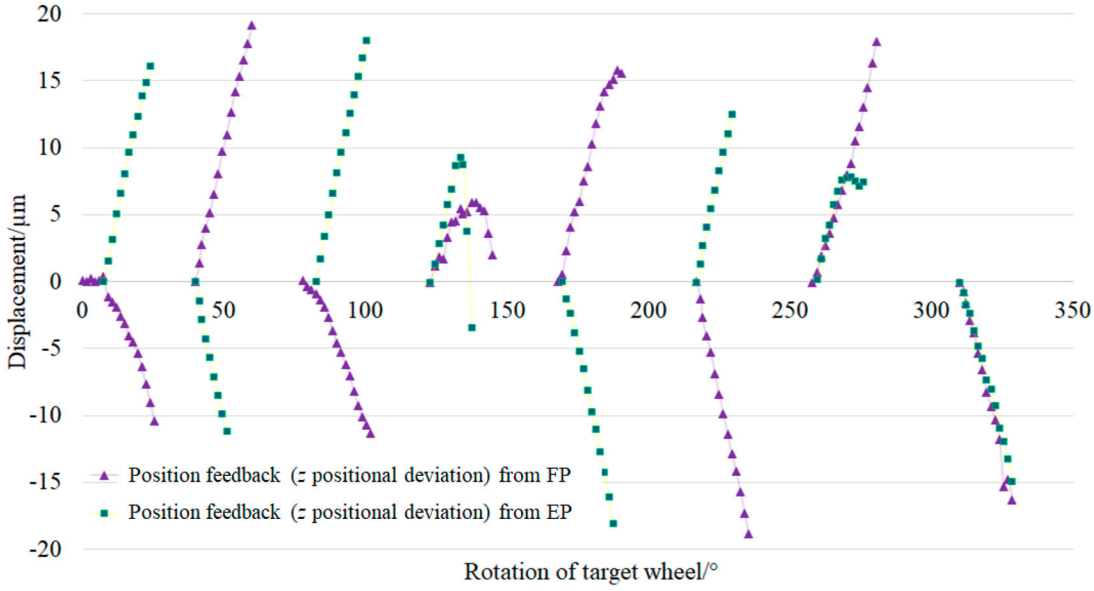

Figure 8. Profiles of the position feedback (*z* positional deviations) for eight locations of the target wheel.

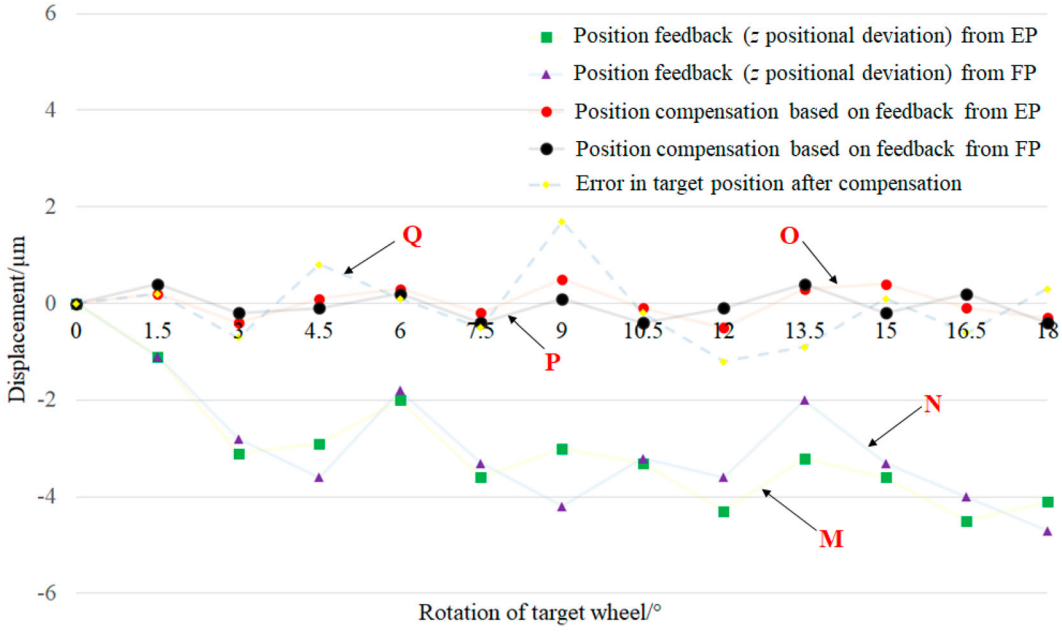

Figure 9. Closed-loop control system in which mirror position setting represents the target position (complaint case).

representing the change of reference plane of the target (i.e. reference orientation of the target). The change of the plane of the target wheel results in the accumulation of the *z* positional deviations of the target at each wheel rotation angle, even though the controller's compensations can reposition the target to the reference position after every 1.5° rotation. Since the target plane needs to be perpendicular to the laser beam in high-power laser operation, the change of the reference orientation of the target during the wheel rotation indicates a serious problem for real-time target alignment for high-repetition rate operation.

From the above discussion, it is clear that the uncertainty in determining the position and orientation of the targets based on the position feedback from EP makes the closed-loop control ineffective in achieving required accuracy (±4 µm) for the real-time target alignment for the high-repetition rate laser operations.

5.3 Investigating the closed-loop design issues using the model

The relation between the positional deviations of the target during the wheel rotation and the sources of the contributing errors can be analysed using the model derived in section 2.2. The model equations (26) to (29) predict the positional deviations of the target for a complete wheel rotation by taking account of the interactions of the following contributing elements: the wheel rotation angle (θ), rotational error motions of the wheel (tip θ_x and tilt θ_y) and the structural parameters of the wheel

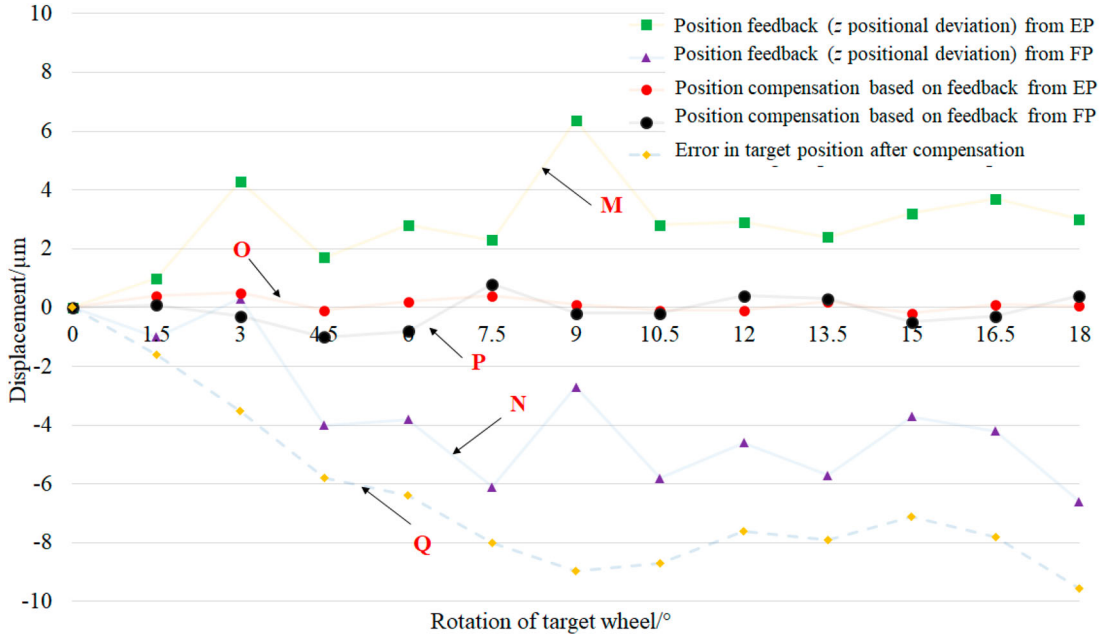

Figure 10. Closed-loop control system in which mirror position setting does not represent the target position (non-complaint case).

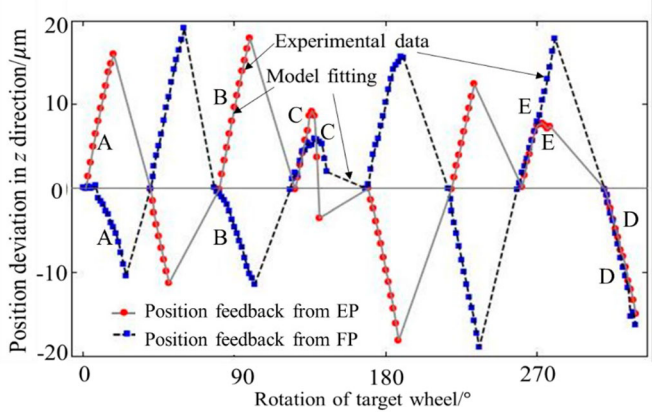

Figure 11. Experimental data (in open loop) and model fitting for both mirror (EP) and target position (FP) settings.

system (wheel diameter y and the offsets, l and h, between the target and the mirror).

The experimental data for the z positional deviations (in open loop) at EP and FP, as shown in Figure 8, was fitted with the periodic function of the model as shown in equations (26) and (30) by letting the θ_x and θ_y angles vary between 0° to 90° (Figure 11). The θ_x and θ_y angles, resulting from the model fitting, are shown in Figures 12 and 13 for EP and FP. The resultant angular error of the wheel α related to θ_x and θ_y, as can be calculated from the equation (28), is shown in Figure 16 and 17. The key observations are the following.

1. Comparative study of Figures 11–13 shows the role of θ_x and θ_y on the magnitude and phase differences of the position feedbacks from EP and FP at different locations of the wheel. Noting that the experimental z positional deviation data are used to calculate θ_x and θ_y of Figure 12 and 13, the differences in the magnitudes of θ_x and θ_y are due to the vertical offset (h) and the horizontal offset (l) between the EP and FP – see equation (32).

2. Comparison of Figures 11–13 also suggests that the θ_x values accumulated with the wheel rotation have greater values than the θ_y values, and the magnitudes of the z position deviation are mainly contributed by θ_x.

3. Based on the magnitude and phase difference of the position feedbacks from EP and FP, the behaviour of the open-loop high-repetition rate system (i.e. wheel rotation) can be fundamentally divided in five categories as shown in Table 1 (identified by A, B, C, D and E profiles in Figures 11–13). As will be seen later that understanding the behaviours of profile A and D as ideal non-complaint and complaint cases, respectively, is necessary to explain the behaviours of profile B, C and E.

4. To understand the nature of the magnitudes and phases of profile *A* and *D* for EP (mirror setting), let's consider the following two cases of equation (30), which is written for EP:

I. $z_{error\ at\ EP} = E_r \sin(\theta + \alpha) = 0$ when no or minimum positional deviations read at EP

$$\text{or}\ \theta = -\alpha \tag{33}$$

II. $\sin(\theta + \alpha) = 1$ when maximum position deviation read at EP

$$\text{or}\ \theta + \alpha = \frac{\pi}{2} \tag{34}$$

Now, consider the wheel rotation for only 1.5°, the 3D shape of the wheel for 1.5°, the path of 1.5° as read by the EP and the associated error motions θ_x and θ_y for 1.5° – as shown in Figure 14 and 15. As can be seen in Figure 14 for case I, the wheel rotation path LK read by EP becomes Ĺ′K′′ due to θ_x and finally ĹK′ due to θ_y. Therefore, ĹK′ represents the effect of resultant angular error α ($\alpha = \tan^{-1}\frac{\sin\theta_x}{\tan\theta_y}$ as shown in equation (28)). ĹK′ approaches to LK (i.e. equation (33)) when θ_x and θ_y are approximately equal in magnitudes, but opposite in directions to cause least positional deviations as read by EP. This behaviour can be

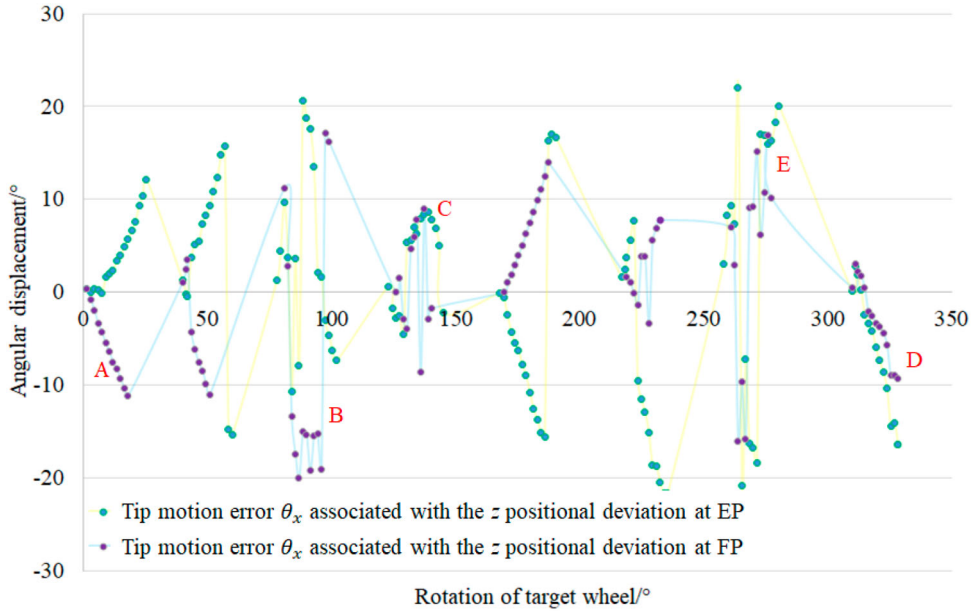

Figure 12. Tip motion error (θ_x) of the wheel calculated from the model fitting.

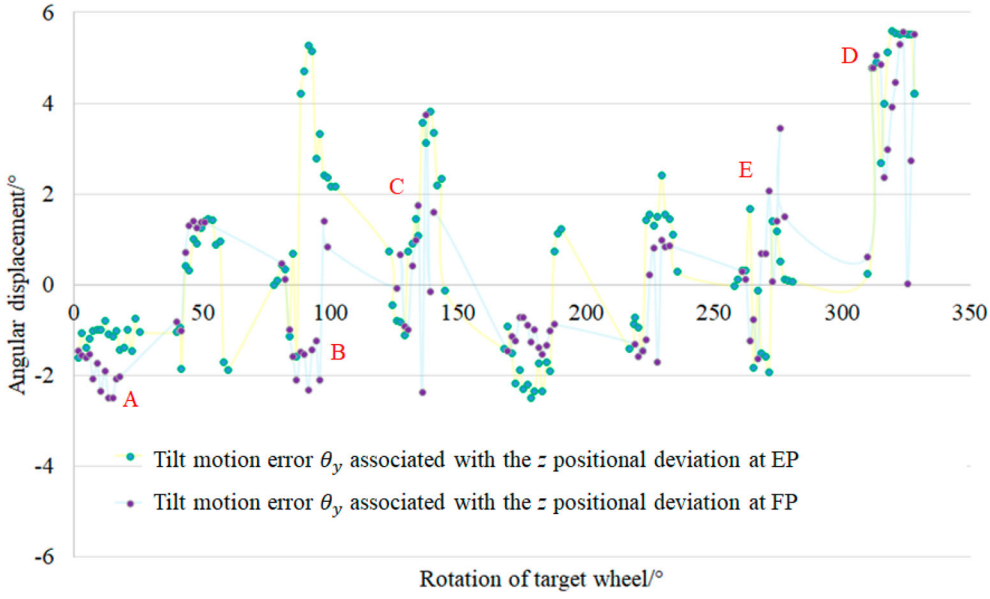

Figure 13. Tilt motion error (θ_y) of the wheel calculated from the model fitting.

observed for small error motions of θ_x and θ_y. Note that the profile *D* for EP of Figure 12 and 13 exhibits the characteristics of case I.

On the other hand, as shown in Figure 15 for case II, ĹK′ will be at maximum angular distance from LK (i.e. equation (34)) when the effect of θ_y is minimum (i.e. θ_x is comparatively much larger than θ_y). The characteristics of case II can be found in the profile *A* for EP in Figure 12 and 13. Also, note the significant shape difference of the IJKL plane of Figure 15 as compared with the plane of Figure 14.

5. After examining the behaviour of EP for minimum and maximum positional deviations scenarios, let's examine the condition at which the positional deviation information from EP and FP should be same (i.e. complaint case). In such case, z_{error} of equation (26) is equal to $z_{error\ at\ M}$ of equation (30). Therefore, from equation (26) and (30), the following can be written:

$$\sin(\theta+\alpha)=\frac{l(\cos\theta_x\cos\theta_y-1)}{h\sqrt{((\sin\theta_y)^2+(\sin\theta_x\cos\theta_y)^2)}} \tag{35}$$

$$\text{or}\quad \theta+\alpha=\sin^{-1}\left(\frac{l(\cos\theta_x\cos\theta_y-1)}{h\sqrt{((\sin\theta_y)^2+(\sin\theta_x\cos\theta_y)^2)}}\right) \tag{36}$$

When, $\cos\theta_x=\frac{1}{\cos\theta_y}$, equation (36) becomes equation (33) for EP. However, $\cos\theta_x=\frac{1}{\cos\theta_y}$ is possible if θ_x and θ_y are small in values and approximately equal. In such case, the position deviation information from EP and FP should be complaint (check the profiles *D* for EP and FP in Figures 11–13).

Table 1. Different categories of behaviour of the open-loop high-repetition rate system (i.e. wheel rotation).

Profile	Magnitudes of the feedback from EP and FP	Phases of the feedback from EP and FP	Note
A	Non-complaint	Non-complaint	180° phase difference between EP and FP
B	Non-complaint	Non-complaint	180° phase difference between EP and FP. Note the random and opposite behaviour of θ_x and θ_y for both EP and FP
C	Approximately complaint	Approximately complaint	Approximately no phase difference between EP and FP. Some random behaviour of θ_x and θ_y for both EP and FP
D	Complaint	Complaint	No phase difference between EP and FP
E	Combination of complaint and non-complaint	Combination of complaint and non-complaint	Compliance of the profiles becomes non-compliance with further wheel rotation

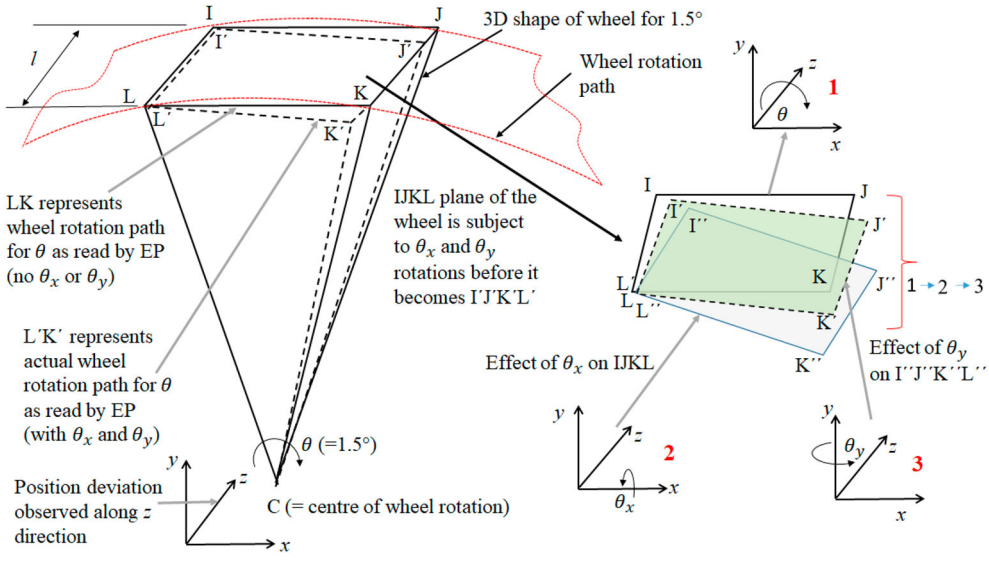

Figure 14. Examination of the wheel rotation path for 1.5° when no or minimum positional deviation read by EP.

Now, when, $(\cos\theta_x \cos\theta_y - 1 = \frac{h\sqrt{((\sin\theta_y)^2+(\sin\theta_x \cos\theta_y)^2)}}{l})$ equation (36) becomes equation (33) for EP. However, $(\cos\theta_x \cos\theta_y - 1)$ is negative, and equation (36) represents 180° phase change with respect to the condition shown in equation (34) for EP. In such case, the positional deviation information from EP and FP will show non-compliance in phase due to the term $l(\cos\theta_x \cos\theta_y - 1)$ of equation (32) or (36), and the magnitude of the positional deviation information from FP will be determined by the equation (32). The profiles of *A* for EP and FP in Figures 11–13 show the characteristics of such non-compliance behaviour, indicating comparatively much larger θ_x with respect to θ_y.

6. Based on the observations of the above 1–5 points, the behaviours of all the five categories of complaint and non-complaint feedback information from EP and FP (Table 1) can be explained. For this purpose, the slopes of the θ_x and θ_y profiles for the five categories (Figure 12 and 13) are taken to calculate the profiles of the resultant angular error α for both EP and FP. The results are shown in Table 2 and Figure 16. Note the changes in the magnitude and the directions of the slopes for the FP profiles with respect to the EP profiles in Table 2, and also the shape difference between any two α profiles for EP and FP in Figure 16. In the absence of a horizontal offset l between EP and FP, the shapes of the α profiles are not expected to change; only the α magnitudes will increase or decrease.

7. The examination of the slopes of the θ_x, θ_y and α profiles of five different categories (*A* to *E*) presented in Table 2 suggests that the compliance between the position feedback from EP and FP depends on two criteria:

- the ratio between two error motions θ_x and θ_y (i.e. $\frac{\theta_x}{\theta_y}$); and
- the change of the resultant angular error α associated with FP with respect to α of EP.

Considering these two criteria, profile *A* and profile *D* show ideal non-complaint and ideal complaint cases, respectively (see Figure 8 and 11). This is based on the observation that if $\frac{\theta_x}{\theta_y}$ has a large value, and the resultant angular error α for FP has a higher value than that for EP, the non-compliant behaviour is expected. As such, for profile A in Table 2, θ_x related to EP (i.e.1.14°) is comparatively much larger than θ_y of the same EP (i.e. −0.02°), which makes $\frac{\theta_x}{\theta_y}$ equal to 57. The interaction of θ_x and θ_y with the offset l generates a resultant angular error α (i.e. 0.09°) for the FP, which is higher than that for the EP (i.e. 0.08°). On the other

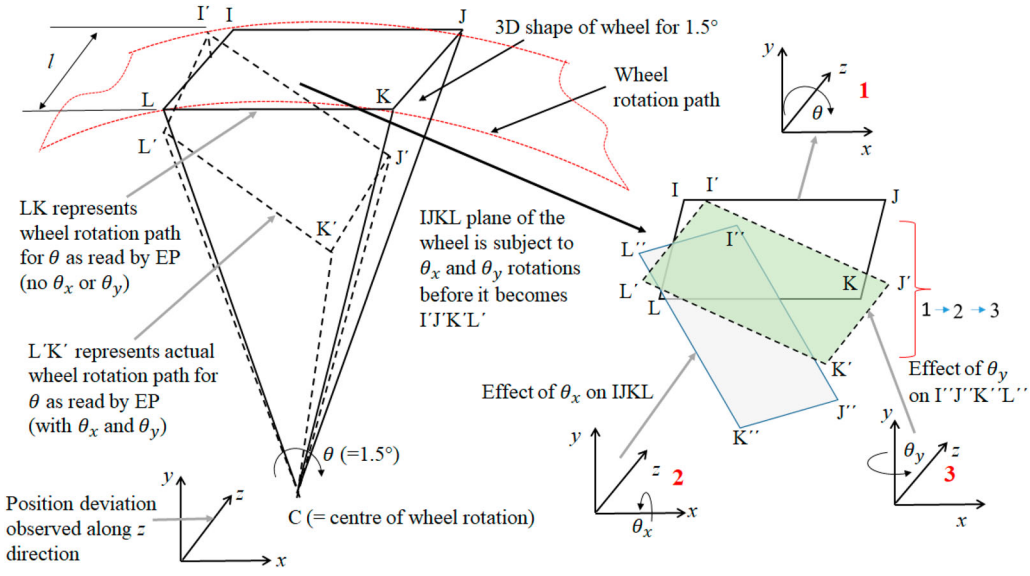

Figure 15. Examination of the wheel rotation path for 1.5° when maximum positional deviation read by EP (note LK and ĹK′ are not shown in perpendicular to each other for the clarity of the figure).

Table 2. Slopes of the θ_x, θ_y and α profiles as shown in Figure 12, 13 and 16.

	EP (mirror setting)			FP (target setting)			
Profile type	θ_x (°)	θ_y (°)	α (°)	θ_x (°)	θ_y (°)	α (°)	Note
A	1.14	−0.02	0.08	−0.89	0.02	0.09	$\lvert\alpha_{FP}\rvert > \lvert\alpha_{EP}\rvert$
B	−2.21	−0.18	−0.02	8.72	0.72	−0.08	$\lvert\alpha_{FP}\rvert > \lvert\alpha_{EP}\rvert$
E	5.26	0.16	0.13	3.72	0.60	−0.01	$\lvert\alpha_{FP}\rvert < \lvert\alpha_{EP}\rvert$
C	−0.80	−0.15	0.23	−1.65	0.32	0.46	$\lvert\alpha_{FP}\rvert > \lvert\alpha_{EP}\rvert$
D	−1.81	−0.32	0.06	−1.24	−0.09	−0.04	$\lvert\alpha_{FP}\rvert < \lvert\alpha_{EP}\rvert$

hand, for profile *D*, θ_x and θ_y have relatively comparable values (−1.81° and −0.32° respectively) for EP, which makes $\frac{\theta_x}{\theta_y}$ equal to 6. In this case, the resultant angular error α (i.e. 0.04°) for the FP is lower than that for the EP (i.e. 0.06°). The behaviours of *B*, *C* and *E* are the combinations of the behaviours of profile *A* and *D*. For example, although it is seen that $|\alpha_{FP}| > |\alpha_{EP}|$ for profile *C*, the result is a complaint case with some anomaly, since $\frac{\theta_x}{\theta_y}$ has lower value (i.e. 5). In contrast, for profile *E*, although it can be seen that $|\alpha_{FP}| < |\alpha_{EP}|$, $\frac{\theta_x}{\theta_y}$ is higher (i.e. 33). Therefore, in this case, the *z* positional deviation at EP shows some compliance with the *z* positional deviation at FP, but eventually the two behaviours become non-complaint (Figure 8 and 11). For profile *B*, with $|\alpha_{FP}| > |\alpha_{EP}|$, the result is a non-complaint case with significant anomaly, since $\frac{\theta_x}{\theta_y}$ is higher (i.e. 12), but not as high as in the case for *A*. A closer look at the slopes of the α profiles of Figure 16 also supports the above observations.

8. In the design of the in-process position measurement system (section 2.1), the EP and FP were positioned aligned to avoid the Abbe errors. However, the reference plane of the wheel changes throughout its rotation due to resultant angular error α ($\alpha = \tan^{-1}\frac{\sin\theta_x}{\tan\theta_y}$). The interaction of the error motions (θ_x and θ_y) with the structural offsets between EP and FP (horizontal offset l and vertical offset h) gives rise to a (1) cosine error in the form of $(l\cos\theta_x\cos\theta_y - l)$ and (1) a sine error in the form of $(\frac{h\sqrt{((\sin\theta_y)^2+(\sin\theta_x\cos\theta_y)^2)}}{\cos\theta}\sin(\theta+\alpha))$ as shown in equation (32). Depending upon the relative values of θ_x and θ_y, these sine and cosine errors cause the target position information from EP either comply or non-comply with the actual target position. In other words, measuring the target position with respect to EP may provide incorrect and non-representative feedback information about the actual target position, representing uncertainty in determining target position for generating compensations by the closed-loop control.

9. Equations (26) and (30) suggest that if the resultant angular error α value can be measured directly at both EP and FP, α will be same for both EP and FP. As can be seen in Figure 16 and 17, the profiles of the resultant angular error α for both EP and FP show similar behaviour. However, as indicated before, the differences in the α values for EP and FP are due to the fact that the experimental *z* positional deviations were used to calculate θ_x and θ_y values, from which α values were determined. Since the *z* positional deviation at FP contains the sine and cosine errors (see equation (32)), the calculated θ_x and θ_y (and hence the α) for FP will be different from those for the EP.

5.4 Improvement of the closed-loop control design

The above discussion suggests that, if the angular errors of the wheel (α) with respect to the reference position and orientation of the target are known for each repetition (described in section 4.1.1), the angular motions (tip *u* and/or tilt *v* about *x* and *y* axes, respectively- see Figure 1) of the tripod of HAMS can be used to generate the angular compensations for α. For this, direct measurement of the angles at or near the target is required, which is

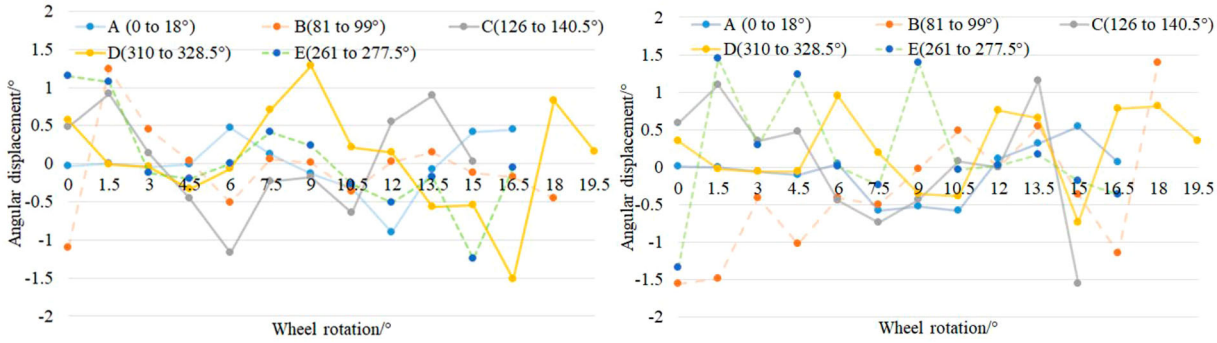

Figure 16. Resultant angular error α for some selective locations of the wheel as calculated from the θ_x and θ_y associated with EP (left) and FP (right).

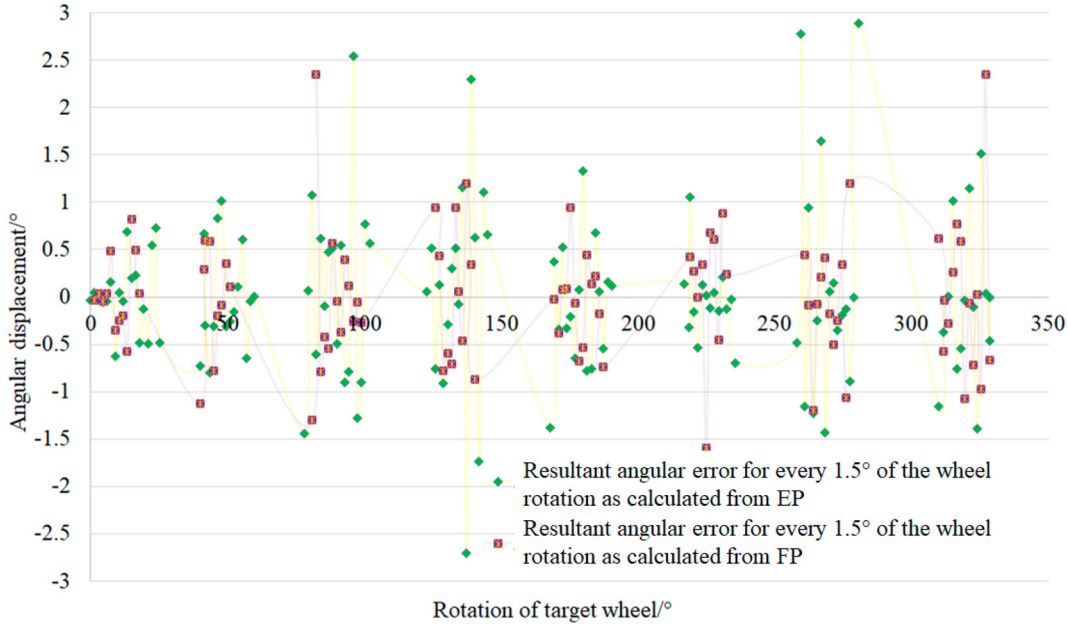

Figure 17. Comparison of the resultant angular errors α of the wheel between two settings as calculated from the information in Figure 12 and 13.

possible with a measurement instrument, such as dual displacement measurement interferometer for both distance and angle (Badami & deGroot, 2013). Alternatively, the z positional deviation at EP measured by the plane mirror interferometer can be used in the motion programme (see Figure 7) to determine the new angular positions of the target, instead of the 'calculated z position' of the motion programme as shown in Figure 7.

Various angular compensation methods were examined by carrying out the experiments described in section 4.1.2 to improve the performance of the closed-loop control. For angular compensation, a simple way to determine the resultant angular error of the wheel (α) was to find an equivalent θ_x angle with the following: position deviation information at EP (mirror position setting) and the distance between the EP to the centre of the wheel (see Figure 3 and 4*a*). The principle behind this strategy is due to the dominant contribution of θ_x in α (see Figures 12, 13, 16 and 17). Figure 18 shows the outcome of applying one such angular compensation scheme, in which the tripod's tip angular motion (u) was used to generate the angular compensation for the equivalent θ_x values. Since the θ_x, which accumulates over time with the wheel rotation, is now compensated, the positional deviation profile of the new scheme (Figure 18) does not show any upward or downward trend as compared with the positional deviation profiles related to the position compensation scheme (Figure 9 or 10). However, the use of equivalent θ_x leaves some errors in the z positional deviation profiles. The zigzag pattern of the position deviation profile in Figure 18 shows the effects of the uncompensated θ_y values. Also, a point to note is that the accuracy of the target position after angular compensation has not improved appreciably as compared with the target positional accuracy achieved by the position compensation scheme (see Figure 9 or 10). This is because, as is described in Karim, Piano, Leach, Branson, et al. (2018) and Karim, Piano, Leach, and Tolley (2018), the tip or tilt motion of the tripod may cause significant positional deviation of the target if the compensation for these positional deviations are not included in the controller as part of a kinematic calibration process.

To overcome the limitation of the above angular compensation scheme and improve the target positional accuracy, another angular compensation scheme is proposed. In this scheme, instead of using the radius of the wheel y, the distance between the centre of the tripod and the EP (mirror position setting) is used to calculate an equivalent θ_x, such that the reference coordinate position of EP always remain the same for all the tip motions (u) of the tripod required to generate the θ_x values for

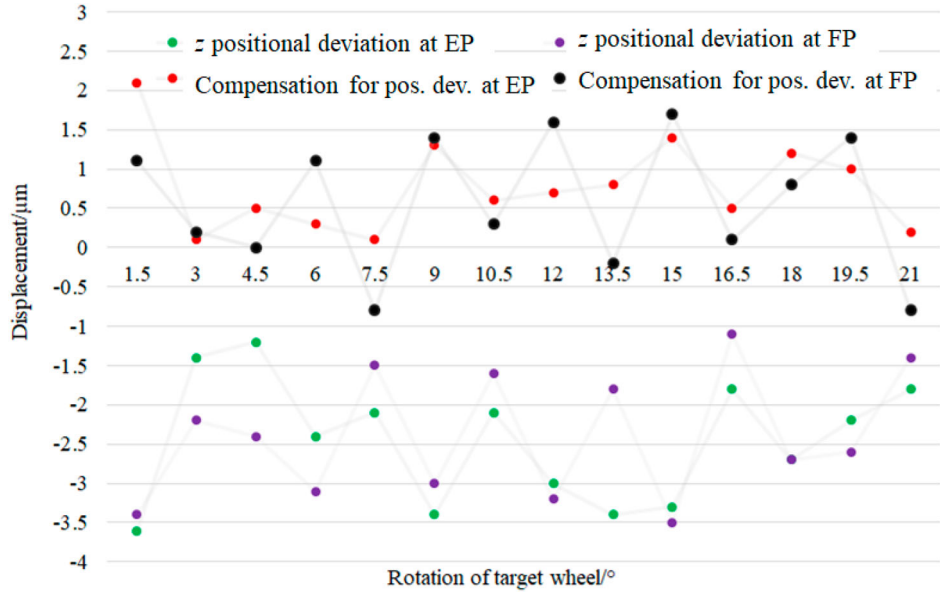

Figure 18. Performance of the improved scheme of the closed-loop control using angular compensation.

the angular compensations. This scheme, in fact, improves the positional accuracy of the target (Figure 19), although it needs further development.

The angular compensation technique for the closed-loop control can provide the following benefits over the positional compensation technique, when considered for real-time target alignment for the high-repetition rate laser operations.

- In angular compensation, true target alignment (both position and orientation of the target), avoiding Abbe errors, is possible since reference position and orientation of the target are maintained throughout the high-repetition rate operation.
- The feedback processing time of the controller for each repetition cycle will be faster for the angular compensation schemes than for the position compensation scheme. This is because the accumulation of the positional deviations of the target with the wheel rotation is small for the angular compensation technique.

5.5 Development of a real-time target position control for high-repetition rate laser operation: outlook

Although the development of an effective closed-loop control solution discussed in this paper is for real-time target alignment for high-repetition rate laser operation, some findings appear to be generally valid for wider precision applications, especially for design considerations of a high-accuracy positioning or measurement system. For example,

(1) To predict the position measurement uncertainty of the end-effector of a positioning system, e.g. a motion stage, which has been designed to avoid the Abbe errors but is subject to a periodic motion, e.g. sinusoidal straightness error of guideways, and its associated rotational error motions (θ_x and θ_y). A high-accuracy positioning system requiring real-time position compensation for the end-effector may become ineffective due to the stated measurement uncertainty.
(2) To predict the positional deviation of the end-effector of a high-repetition rate positioning system if the error motions and the structural parameters (see the model equations (26), (30), (32) etc) are known.
(3) Based on the positional deviation equations of the model, to construct a position compensation table which can be included in the controller of the positioning system to carry out pre-calibrated error compensation for the end-effector.
(4) To develop a real-time position control of the end-effector based on angular compensation technique to avoid Abbe error and maintain the reference position and orientation of the end-effector of a positioning system.

Furthermore, since the FP and EP will not be the same for many applications (e.g. high accuracy positioning system) and, therefore, there may be some uncertainties in determining the actual target position information from the sensor, the only way to estimate this uncertainty is by modelling the particular scenario of the application, with the considerations of its key characteristic parameters such as the kinematic errors associated with the motions of the positioning system, the spatial offsets between the EP and FP, to understand the effect of the position uncertainty in the control system's behaviour as shown in this paper.

5.6 Future work

The future work in the area of developing a closed-loop system for real-time target alignment involves further improvement of the angular compensation techniques to increase the target position accuracy for higher repetition rate operations (> 0.5 Hz).

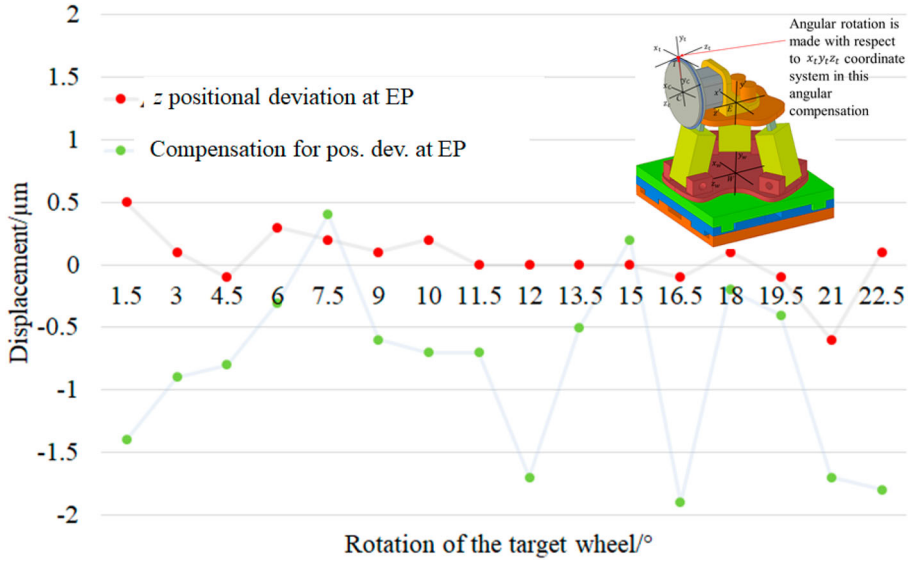

Figure 19. Performance of the improved closed-loop control using different approach to angular compensation.

While this paper outlines the tuning of the control system design and its implementation for addressing the non-collocation issue of the target (FP) and the sensor (EP), the paper has not covered the study of the positional uncertainty of the target, arising from the non-collocation issue, under a closed-loop control which may be subject to instability due to external disturbances, e.g. vibration. This important study is considered as the next major stage of the current research presented in this paper, so that a robust control strategy can be developed to simultaneously accomplish the desired disturbance rejection performance and maintain a reference position and orientation of the target by avoiding the uncertainty in determining the actual position of the target in 3D space.

Case-studies will also need to be carried out to evaluate the applicability of the model and the findings of this paper for such precision applications that require high positional accuracy of the target.

6. Conclusion

For the target positioning system for high-power high-repetition rate laser operation, real-time target position control is required for the accurate repositioning of the target (especially, in the z direction along the laser axis) at the reference target position. A closed-loop control, commonly used for actuator control, can fulfil this requirement. However, getting accurate and reliable feedback of the target position for the controller poses a significant challenge. One of the main reasons for this is due to the inclusion of Abbe errors to the target position measurement, since the functional point (target) and the effective point (where the target position is actually measured) are often not same. This paper presents a closed-loop control method for a high-repetition rate target positioning system (a target interface wheel controlled by the motion stages of a hybrid mechanism) based on a target position measurement system designed to avoid Abbe errors. A plane mirror interferometer is used as the sensor, and the target position feedback is used by the controller of the motions stages to generate the compensations for the positional deviation of the target in the z direction. The plane mirror (effective point) is placed at a location on the wheel as close to the target (functional point) as practical, with the smallest possible offsets between the two points.

The experimental results of the closed-loop control method show that, while the control system is capable of repositioning the targets within ± 1.7 μm of the reference target position during the wheel rotation, this is not the case for all the locations of the targets whose positions are to be determined by the corresponding effective points of the plane mirror. The nonlinear position data at different locations of the wheel causes magnitude and phase differences (direction) between the position feedback (i.e. z positional deviation) from the target and the effective point at various locations of the target, resulting in inaccurate position compensations generated by the controller.

To understand the cause of the errors in the position feedback of the control system, a model was developed to find the relationship between the target position feedback (i.e. z positional deviation) and the errors affecting the feedback accuracy. Fitting the experimental data of the z positional deviations (in open-loop control) into the model's equations suggests that two criteria are important to determine the magnitude and phase differences between the feedback from the target and the effective point: (1) the relative magnitudes of the wheel's rotational error motions, which determine the resultant angular error of the wheel, associated with the effective point and (2) the change of the resultant angular error of the target with respect to that of the effective point. To overcome the closed-loop feedback problem, a solution is proposed where the controller generates the angular compensations based on the resultant angular errors calculated from the z positional deviation at the effective point (mirror). With this approach, a positional accuracy of ± 1 μm is achieved, while it is possible to maintain the target's reference plane throughout the wheel rotation and, hence, avoid the Abbe error for the target position measurement.

The model and the observations of this paper are general and applicable to wider precision applications that require high

positional accuracy. Typical applications may include: (1) the prediction of the uncertainty related to the position measurement of the target of a positioning system in the presence of periodic error/s (i.e. straightness error) that may arise from the drive system of the motion stage/s, and (2) the generation of an effective solution for the real-time position and orientation control of targets for a process requiring high-repetition rate operation.

Acknowledgements

This research project is jointly funded by STFC (Oxfordshire, UK) and EPSRC (grants EP/M008993/1 and EP/L016567/1).

Disclosure statement

No potential conflict of interest was reported by the authors.

Funding

This work was supported by Engineering and Physical Sciences Research Council: [Grant Number EP/L016567/1]; Science and Technology Facilities Council: [Grant Number EP/M008993/1].

References

Badami, V. G., & deGroot, P. J. (2013). Displacement measuring interferometry. In K. Harding (Ed.), *Handbook of optical dimensional metrology* (pp. 157–239). CRC Press.

Booth, N., Clarke, R., Heathcote, R., Neely, D., Pattathil, R., Rusby, D., Spindloe, C., Symes, D., Tolley, M. K., & Tomlinson, S. (2014). High-rep rate target development for ultra-intense interaction science at the central laser facility. *Proceedings SPIE*, *9211*, 1–8. https://doi.org/10.1117/12.2061803

Bosmans, N., Qian, J., & Reynaerts, D. (2017). Design and experimental validation of an ultra-precision Abbe-compliant linear encoder-based position measurement system. *Precision Engineering*, *47*, 197–211. https://doi.org/10.1016/j.precisioneng.2016.08.005

Bruant, I., Gallimard, L., & Nikoukar, S. (2010). Optimal piezoelectric actuator and sensor location for active vibration control using genetic algorithm. *Journal of Sound and Vibration*, *329*(10), 1615–1635. https://doi.org/10.1016/j.jsv.2009.12.001

Bryan, J. (1979). The Abbe principle revisited: An updated interpretation. *Precision Engineering*, *1*(3), 129–132. https://doi.org/10.1016/0141-6359(79)90037-0

Buice, E. S. (2018). Alignment and assembly principles. In R. K. Leach & S. T. Smith (Eds.), *Basics of precision engineering* (pp. 449–492). CRC Press.

Colledani, M., Tolio, T., Fischer, A., Lung, B., Lanza, G., Schmitt, R., & Vancza, J. (2014). Design and management of manufacturing systems for production quality. *CIRP Annals – Manufacturing Technology*, *63*(2), 773–796. https://doi.org/10.1016/j.cirp.2014.05.002

Delta Tau Data System Inc. (2008). *Turbo PMAC user manual: Programmable multi-axis controller*. Author.

Gao, Y., Bin, J., Haffa, D., Kreuzer, C., Hatmann, J., Speicher, M., Lindner, F. H., Ostermayr, T. M., Hilz, P., Rosch, T. F., Lehrack, S., Englbrecht, F., Seuferling, S., Gilljohann, M., Ding, H., Ma, W., Parodi, K., & Schreiber, J. (2017). An automated 0.5 Hz nano-foil target positioning system for intense laser plasma experiments. *High Power Laser Science and Engineering*, *5*(12). https://doi.org/10.1017/hpl.2017.10

Gao, W., Haitjema, H., Fang, F. Z., Leach, R. K., Cheung, C. F., Savio, E., & Linares, J. M. (2019). On-machine and in-process surface metrology for precision manufacturing. *CIRP Annals – Manufacturing Technology*, *68*(2), 843–866. https://doi.org/10.1016/j.cirp.2019.05.005

Hansen, H. N., Carneiro, K., Haitijema, H., & Chiffre, L. D. (2006). Dimensional micro and nano metrology. *CIRP Annals*, *55*(2), 721–743. https://doi.org/10.1016/j.cirp.2006.10.005

Karim, S., Piano, S., Leach, R. K., Branson, D., & Tolley, M. (2018, November 4–9). *Calibration and adjustment of high-precision five degree of-freedom hybrid mechanism* [Paper presentation]. 33rd Annual Meeting ASPE, Las Vegas, USA.

Karim, S., Piano, S., Leach, R. K., & Tolley, M. (2018). Error modelling and validation of a high-precision five degree of freedom hybrid mechanism for high-power high-repetition rate laser system. *Precision Engineering*, *54*, 182–197. https://doi.org/10.1016/j.precisioneng.2018.04.018

Ramesh, R., Mannan, M., & Poo, A. (2000). Error compensation in machine tools — a review. *International Journal of Machine Tools and Manufacture*, *40*(9), 1257–1284. https://doi.org/10.1016/S0890-6955(00)00010-9

Ruijl, T. (2001). Ultra precision coordinate measuring machine-design, calibration and error compensation. [Unpublished doctoral dissertation]. Delft University.

Sartori, S., & Zhang, G. X. (1995). Geometric error measurement and compensation of machines. *Annals of the CIRP*, *44*(2), 599–609. https://doi.org/10.1016/S0007-8506(07)60507-1

Schmidt, R. M., Schitter, G., Rankers, A., & Eijk, J. V. (2014). *The design of high performance mechatronics*. Delft University Press.

Schmitt, R., Mallmann, G., Winands, K., & Pothen, M. (2012). Inline process metrology system for the control of laser surface structuring processes. *Physics Procedia*, *39*, 814–822. https://doi.org/10.1016/j.phpro.2012.10.105

Schmitt, R., Mallmann, G., Winands, K., & Pothen, M. (2013). Automated process initialization of laser surface structuring processes by inline process metrology. *Physics Procedia*, *41*, 887–895. https://doi.org/10.1016/j.phpro.2013.03.163

Schwenke, H., Knapp, W., Haitjema, H., Weckenmann, A., Schmitt, R., & Delbressine, F. (2008). Geometric error measurement and compensation of machines—An update. *CIRP Annals – Manufacturing Technology*, *57*(2), 660–675. https://doi.org/10.1016/j.cirp.2008.09.008

Seugling, R. M. (2018). System modelling. In R. K. Leach & S. T. Smith (Eds.), *Basics of precision engineering* (pp. 369–412). CRC Press.

Slocum, A. H. (1992). *Precision machine design*. Prentice-Hall.

Spindloe, C., Tolley, M. K., Hiscock, P., Beardsley, M., & Spencer, J. J. (2011). An update of target fabrication techniques for the mass production of advanced fast ignition cone targets. *Fusion Science Technology*, *59*(1), 221–226. https://doi.org/10.13182/FST11-A11528

Syam, W. P., Rybalcenko, K., Gaio, A., Crabtree, J., & Leach, R. K. (2019). Methodology for the development of in-line surface measuring instruments with a case study for additive surface finishing. *Optical Lasers Engineering*, *121*, 271–288. https://doi.org/10.1016/j.optlaseng.2019.04.015

Symes, D. R., Booth, N., Baraclough, M., Indorf, G., Oliver, P., Scott, G. G., Neely, D., Spindloe, C., Heathcote, R. I., Clarke, R. J. P., Foster, S., Gregory, C. D., & Rajeev, P. P. (2014). Progress on positioning of solid targets for Gemini. *Central Laser Facility Annual Report*, *15*. https://www.clf.stfc.ac.uk/Pages/ar14-15_Development_Symes_Targetpositioning.pdf

Tolley, M., & Spindloe, C. (2013). Microtargetry for high power lasers in laser-plasma interactions. In P. Mckenna, D. Neely, R. Bingham, & D. A. Jaroszynski (Eds.), *Laser-plasma interactions and applications* (pp. 431–459). Springer.

Yang, S. M., & Lee, Y. J. (1993). Optimisation of noncollocated sensor/actuator location and feedback gain in control systems. *Smart Materials and Structure*, *2*(2), 96–102. https://doi.org/10.1088/0964-1726/2/2/005

Yang, S. M., & Zhang, G. F. (2018). A review on interferometry for geometric measurement. *Measurement Science and Technology*, *29*(10), 102001. https://doi.org/10.1088/1361-6501/aad732

Appendix 1

$A_1, A_2, A_3, B_1, B_2, B_3, C_1, C_2, C_3, D_1$ and D_2, as shown below, represent the elements of the matrix in equation (12) of section 2.2:

$$A_1 = \cos\theta\cos(\theta_y - \theta_m) + \sin\theta\sin\theta_x\cos(\theta_y + \theta_m) - \cos\theta, \qquad (13)$$

$$A_2 = \sin\theta + \cos\theta \sin\theta_y sin(\theta_y + \theta_m) + \sin\theta(\cos\theta_n \cos\theta_x - \sin\theta_x \sin\theta_n \cos(\theta_y - \theta_m)), \quad (14)$$

$$A_3 = \sin\theta(\cos\theta_x \sin\theta_n + \sin\theta_x \cos\theta_n \cos(\theta_y - \theta_m)) - \cos\theta \cos\theta_n \sin(\theta_y - \theta_m), \quad (15)$$

$$B_1 = \cos\theta \sin\theta_x \sin(\theta_y + \theta_m) - \sin\theta \cos(\theta_y - \theta_m) - \sin\theta, \quad (16)$$

$$B_2 = \cos\theta(\cos\theta_n \cos\theta_x - \sin\theta_x \sin\theta_n \cos(\theta_y - \theta_m)) - \sin\theta \sin\theta_n \sin(\theta_y + \theta_m) - \cos\theta, \quad (17)$$

$$B_3 = \sin\theta \cos\theta_n \sin(\theta_y + \theta_m) + \cos\theta(\cos\theta_x \sin\theta_n + \sin\theta_x \cos\theta_n \cos(\theta_y - \theta_m)), \quad (18)$$

$$C_1 = \cos\theta_x \sin(\theta_y + \theta_m), \quad (19)$$

$$C_2 = -\cos\theta_n \sin\theta_x - \cos\theta_x \sin\theta_n \cos(\theta_y - \theta_m), \quad (20)$$

$$C_3 = \cos\theta_x \cos\theta_n \cos(\theta_y - \theta_m) - \sin\theta_n \sin\theta_x - 1, \quad (21)$$

$$D_1 = s(\cos\theta \sin(\theta_y - \theta_m) + \sin\theta \sin\theta_x \sin(\theta_y + \theta_m) - s\cos\theta - (h + y)(\sin\theta \cos(\theta_y - \theta_m) - \cos\theta \sin\theta_x \sin(\theta_y + \theta_m)) - (h + y)\sin\theta + l\cos\theta_x \sin(\theta_y + \theta_m), \quad (22)$$

$$D_2 = s\sin\theta - (h + y)\cos\theta - (h + y)(\sin\theta \sin\theta_n \sin(\theta_y + \theta_m) - \cos\theta(\cos\theta_y \cos\theta_x - \sin\theta_x \sin\theta_y \cos(\theta_y - \theta_m)) + s(\cos\theta \sin\theta_y \sin(\theta_y + \theta_m) + \sin\theta(\cos\theta_n \cos\theta_x - \sin\theta_x \sin\theta_n \cos(\theta_y - \theta_m)) - l(\cos\theta_y \sin\theta_x + \cos\theta_x \sin\theta_y \cos(\theta_y - \theta_m)). \quad (23)$$